Chapter 3
Visualization of Intracellular Elements Using Scanning X-Ray Fluorescence Microscopy

Mari Shimura, Lukasz Szyrwiel, Satoshi Matsuyama, and Kazuto Yamauchi

Abstract Recent technological developments have enabled the imaging of chemical elements in cells, although quantitative analyses, such as by inductively coupled plasma mass spectrometry, were developed previously. Applications allowing high-resolution imaging at the single-cell level are anticipated in cell biology and medicine, where the roles of elements, especially in relation to intracellular molecules such as proteins, nucleic acids, lipids, and sugars, are essential for understanding cellular functions. The expression of proteins and genes varies depending on cellular function, and multiple elements are likely to be associated with biological molecules in the functioning of cell proliferation, differentiation, aging, and stress responses. In this review, we describe a scanning X-ray fluorescence microscopy system, which can reliably determine the cellular distribution of multiple elements by a sub-100-nm focusing approach, together with its applications. Visualizing intracellular elements and understanding their dynamics at the single-cell level may provide great insight into their behaviors.

Keywords X-ray microscopy • Single-cell level • Intracellular element • Labeling • Synchrotron • X-ray fluorescence analysis

M. Shimura (✉)
Department of Intractable Diseases, Research Institute, National Center for Global Health and Medicine, Shinjuku, Tokyo 162-8655, Japan

RIKEN SPring-8 Center, 1-1-1 Kouto, Sayo, Hyogo 679-5148, Japan
e-mail: mshimura@ri.ncgm.go.jp

L. Szyrwiel
RIKEN SPring-8 Center, 1-1-1 Kouto, Sayo, Hyogo 679-5148, Japan

CNRS/UPPA, LCABIE, UMR5254, F-64053 Pau, France

Department of Chemistry of Drugs, Wrocław Medical University, ul. Borowska 211, 50-552 Wrocław, Poland

S. Matsuyama • K. Yamauchi
Department of Precision Science and Technology, Graduate School of Engineering, Osaka University, Suita, Osaka 565-0871, Japan

© Springer Japan KK 2017

Y. Ogra, T. Hirata (eds.), *Metallomics*, DOI 10.1007/978-4-431-56463-8_3

3.1 Imaging Intracellular Elements at the Single-Cell Level Provides New Insights

Imaging provides information, such as on the pattern and distribution of molecules, which is essential to understand the characteristics of objects that cannot be determined by measuring element concentrations. Light microscopy, fluorescence microscopy, and electron microscopy have been widely used to reveal cellular functions. Recently, technologies for imaging elements in cells have been established, such as laser ablation inductively coupled plasma mass spectrometry (LA-ICP-MS), microparticle-induced X-ray emission (PIXE), and X-ray fluorescence microscopy (XRF) [1–5]. Their applications in biology and medicine have often been reported, but a high resolution is required to observe the distribution of elements intracellularly at the single-cell level. Previous findings on proteins and nucleic acids indicate that cells are not a homogeneous population. For example, cell growth proceeds via different stages of the cell cycle (Fig. 3.1, cell cycle). Cell division also occurs, which is a dynamic process in which proteins and nucleic acids are produced and exhibit complex changes in their formations. Previous findings suggested that intracellular elements are related to cell proliferation [6, 7] and may undergo changes in their intracellular distribution. In addition, cancer cells often

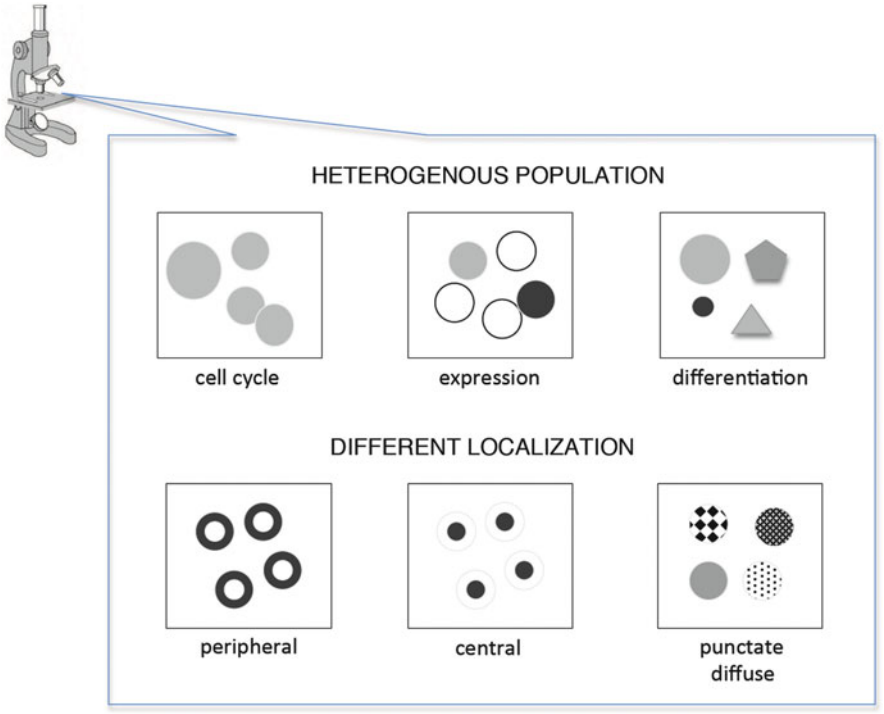

Fig. 3.1 Imaging intracellular elements at the single-cell level provides new insights

exhibit genetic variation, showing different protein expression levels within a population, which has been observed by flow cytometry (Fig. 3.1, expression). Normal cell populations are more quiescent, but they also differentiate and age (Fig. 3.1, differentiation). In these various processes, molecules in cells may exhibit different distributions, such as peripheral, focal, punctate, or diffuse (Fig. 3.1, different localizations). These different distributions suggest different binding partners, which is probably similar in the case of elements, since some essential elements are associated with proteins or nucleic acids [8, 9]. Imaging technology is also useful in the medical field. Imaging a series of sections using different staining procedures can be informative despite the small volume studied. Imaging of multiple intracellular elements may have the potential to clarify unknown disease mechanisms. In this chapter, we introduce our developed method of scanning X-ray fluorescence microscopy (SXFM), which has been especially established for imaging cells at the single-cell level.

3.2 Scanning X-Ray Fluorescence Microscopy

SXFM (also abbreviated as μXRF) is a very powerful tool that can quantitatively and nondestructively measure the distributions of elements with high sensitivity. As a result, it is widely applied in many industries and scientific fields and even in the fields of art and archeology [10]. There are a range of SXFM apparatuses, from compact systems that are commercially available to large systems installed at special facilities. A schematic of a typical apparatus is shown in Fig. 3.2. A typical

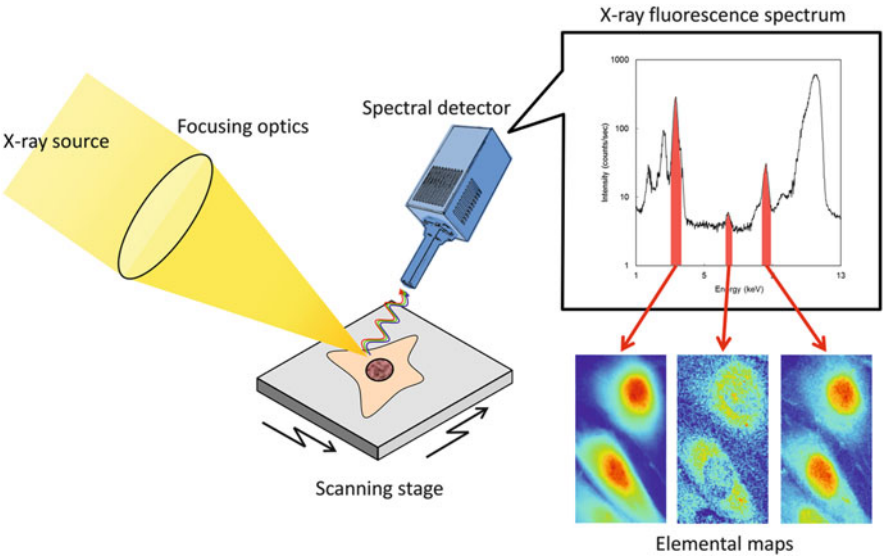

Fig. 3.2 Schematic of a scanning X-ray fluorescence microscope (SXFM)

system consists of an X-ray source, focusing optics, a sample scanner, and a detector to acquire X-ray spectra. In this context, the following question arises: What are the requirements for single-cell imaging? The most important features are an X-ray source with intense brightness and high-quality X-ray focusing optics.

3.2.1 Synchrotron Radiation X-Ray Source

An X-ray tube is a very common X-ray generator at the laboratory scale that can produce X-rays via collisions between accelerated electrons of several tens of kilovolts and a material, usually tungsten, molybdenum, or copper. However, it is too weak and has too large a source size and divergence for SXFM at the single-cell level. A synchrotron radiation (SR) X-ray source (Fig. 3.3, left) was developed to overcome these issues. Electrons traveling almost at the speed of light (99.9999998 % of light speed when an electron has energy of 8 GeV) can produce X-rays when they are bent by a magnetic field (Fig. 3.3, right). The produced X-rays are over a billion times as intense as an X-ray tube. This is advantageous because generally the sensitivity is proportional to the intensity of input X-rays. In addition, the X-ray source size and divergence are very small, which leads to the formation of an intense focused beam because the demagnification of practical focusing optics is limited. The typical values expressed as the standard deviation are 300 μm (H) × 7 μm (V) and 13 μrad (H) × 4 μrad (V) in the SPring-8 (Hyogo, Japan) standard undulator X-ray source [11].

3.2.2 X-Ray Focusing Optics

One of the difficulties for scanning-type X-ray microscopes is the development of X-ray focusing optics. This is due to the tolerance of fabrication error being very limited because the acceptable size of fabrication errors decreases with a decrease

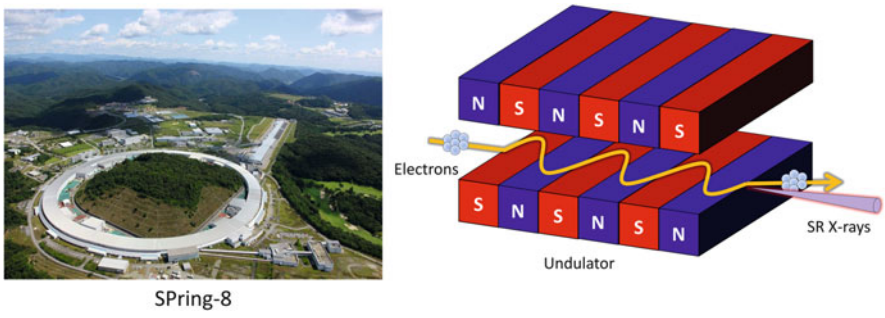

Fig. 3.3 *Left*, photograph of SPring-8; *right*, X-ray generation at a synchrotron radiation facility

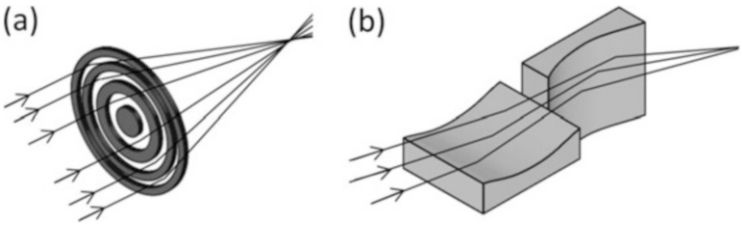

Fig. 3.4 Schematic of (**a**) Fresnel zone plate and (**b**) Kirkpatrick-Baez mirrors

in the wavelength of light. In addition, we cannot utilize a conventional lens, often used in the visible light region, as X-ray focusing optics because the refractive index in the X-ray region is less than but very close to 1 (e.g., refractive index of gold at 10 keV = 0.99997). Specialized focusing optics for X-rays is essential. Currently, Fresnel zone plates and Kirkpatrick-Baez (KB) mirrors are often used as practical and high-performance X-ray focusing optics (Fig. 3.4). A Fresnel zone plate is a circular diffraction grating with unequally spaced periods. It has major advantages in terms of usability and quality. However, its throughput is not very high because only the first-order diffracted light is used for focusing. In addition, diffraction significantly depends on the wavelength, which results in achromatic aberration. On the other hand, KB mirrors are focusing optics that utilize the phenomenon of total reflection. They consist of two elliptical mirrors arranged perpendicular to each other to focus X-rays two-dimensionally. Owing to the separation of the mirrors in the vertical and horizontal directions, almost planar mirrors that can be fabricated with extreme precision can be used as focusing mirrors. The benefits of this approach are high throughput, large acceptance, and no chromatic aberration. However, it has the disadvantages of difficult mirror fabrication, high cost, and difficult mirror adjustment. The former can be explained using an equation that can calculate acceptable figure errors on an X-ray mirror to reach the theoretically minimum spot (diffraction limit):

$$d = \frac{\lambda}{8 \sin\theta}$$

where λ is wavelength and θ is grazing-incidence angle. Typical d at 10 keV is ~4 nm. This accuracy is very severe, even using state-of-the-art precision machining. To realize SXFM with high resolution and high sensitivity, we developed high-quality KB mirror optics [12]. The mirrors were superpolished by the elastic emission machining (EEM) technique [13], which can realize nanometer-level shape accuracy and an atomically smooth surface. The achieved shape accuracy is 2 nm (Fig. 3.5), which is sufficiently small to satisfy the accuracy requirements. Focusing tests conducted at SPring-8, a synchrotron radiation facility in Japan (Fig. 3.3, left), revealed that our focusing system could focus X-rays down to an almost diffraction-limited spot size of 48 (H) nm × 36 (V) nm at X-ray energy of 15 keV (Fig. 3.5) [14]. In addition, owing to the smooth surface, loss of reflectivity

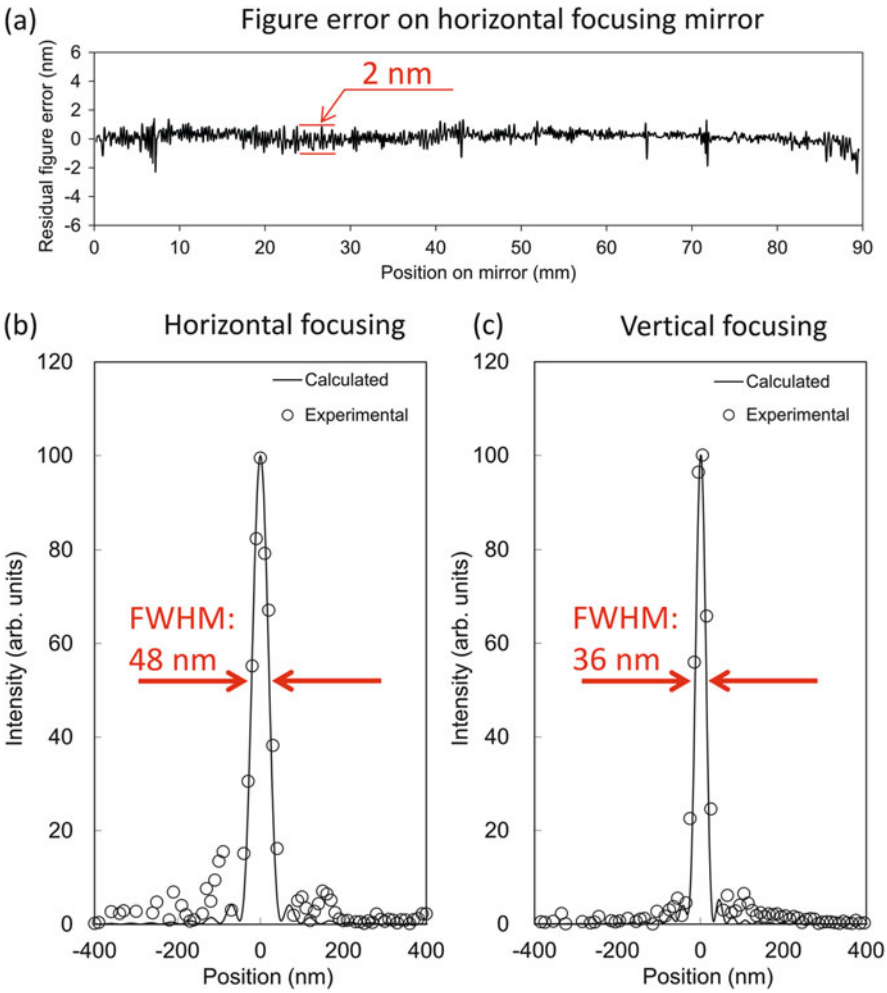

Fig. 3.5 Performance of fabricated Kirkpatrick-Baez mirrors. (**a**) Figure error on the horizontal focusing mirror used. (**b**, **c**) Measured beam profiles at the focus

was almost zero. Thus, we could successfully develop a focusing system that is highly suitable for SXFM.

3.2.3 Demonstration of SXFM Performance

The prototype for our SXFM was developed at BL29XUL of SPring-8 (Fig. 3.6). The system consisted of the KB focusing system, a detector system including a silicon drift detector (SDD), a fast multichannel analyzer (MCA), and a fine stage

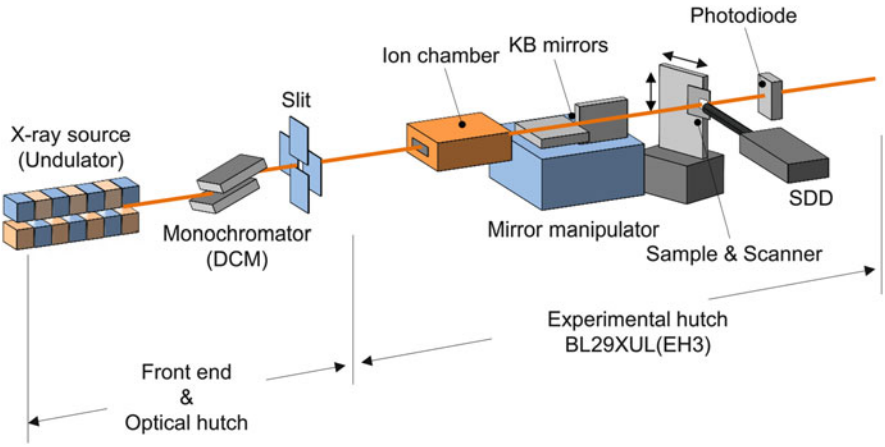

Fig. 3.6 Schematic of SXFM system

for sample scanning. The spectra formed by the MCA are recorded for every pixel over the measurement area to select chemical elements to be visualized after measurement and to process noise reduction and peak fitting. To demonstrate the performance, a fine test pattern, fabricated with a focused ion beam figuring system, was observed [12]. To find regions of interest effectively, first, a wide beam with a width of 1000 nm and then a 40-nm beam were used. This beam broadening could be adjusted using a slit placed downstream of the undulator X-ray source, in which the beam size is controllable between the diffraction limit (30×50 nm^2) and ~1000 nm. The distributions of elements were gradually magnified, and finally the target area was found. As can be seen in the gallium maps in Fig. 3.7, a 50-nm line width was successfully visualized.

Next, as a test of practical cell imaging, cultured mouse cells with mitochondria labeled with fluorescein isothiocyanate and gold colloids were observed [15]. The cells supported on a thin polymer film were chemically fixed with paraformaldehyde and dehydrated with ethanol. The obtained element maps are shown in Fig. 3.8. The right panel is a magnified image of the region of interest shown by the white square in the left panel in this figure. The color scale shows the semiquantitatively determined levels of elements in the irradiated area. A calibration curve for the semiquantitative analysis was made using the fluorescence signals from platinum films, in which the element levels were determined in advance. The SXFM provided various element maps, such as for phosphorus, sulfur, chlorine, calcium, iron, copper, zinc, and gold. The gold maps indicated the locations of mitochondria. Interestingly, zinc, and probably copper, seemed to be distributed in the mitochondria and nucleus. The obtained distributions of elements suggest that the SXFM system can visualize the distributions of multiple trace elements at the single-cell level. The detection limits were estimated from various observation results. Detection limits tend to increase with a decrease of atomic number because of the decreases of absorption and fluorescence yield. Typical detection limits of

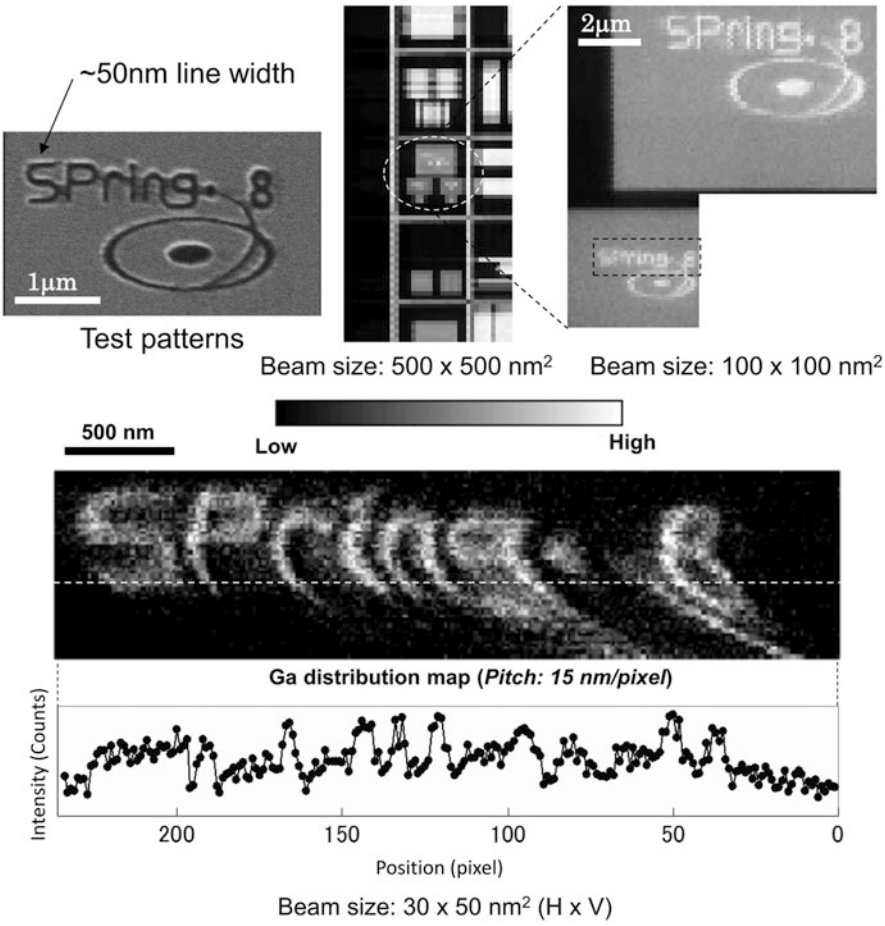

Fig. 3.7 High-resolution gallium maps of a test pattern. X-ray energy = 15 keV (The figure is taken from Matsuyama et al. 2006, with permission [12])

our SXFM are as follows, which depends on sample preparation, sample thickness, supporting membrane, and coexisting elements within a sample: Si (1 fg), P (0.4 fg), S (0.2 fg), Cl (0.3 fg), Ca (0.03 fg), Fe (0.01 fg), Cu (0.004 fg), Zn (0.005 fg), Ga (0.009 fg), W (0.01 fg), and Au (0.009 fg) [16]. The smallest spatial resolution was 30 nm, although there is a trade-off between spatial resolution and sensitivity. This is because the achievable minimum beam size can be obtained only when the X-ray source size is limited to 10 μm by a slit. In this case, beam intensity decreases with a decrease in the area of the source. Even current SR X-ray sources are not sufficiently small for such applications, although they are much better than an X-ray tube. Improvements of the sensitivity and spatial resolution are thus problems that remain to be resolved. An approach for achieving this is described in "Future SXFM."

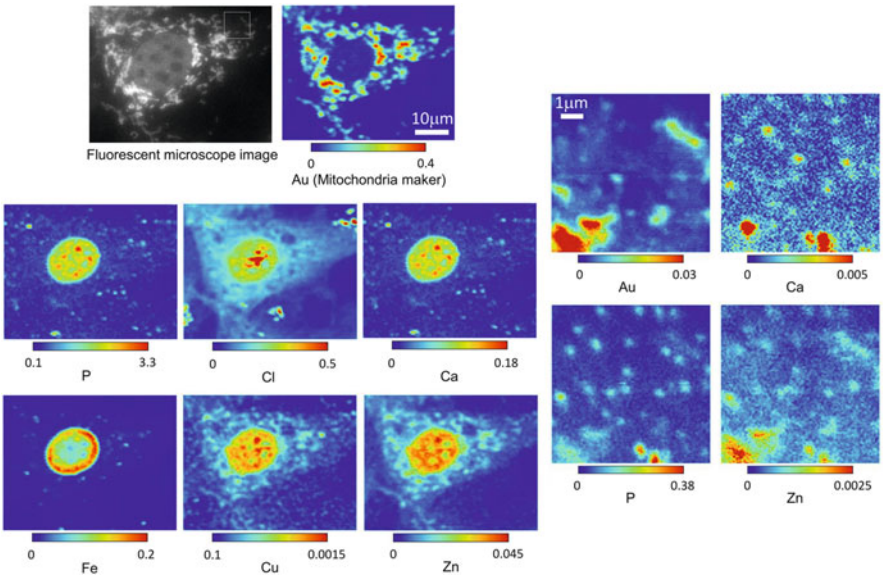

Fig. 3.8 Intracellular element maps of a whole cell (*left*) and the high-resolution element maps (*right*). Parameters of the *left* images: exposure = 1 s/pixel, scanning step = 500 nm/pixel, and X-ray energy = 15 keV. Parameters of the *right* images: exposure = 2 s/pixel, scanning step = 70 nm/pixel, and X-ray energy = 15 keV. *Color bars* indicate the elemental contents (fg) in an irradiation area (The figure is taken from Matsuyama et al. 2009, with permission [15])

3.3 Applications in Biology and Medicine

3.3.1 SXFM Is Now User-Friendly

To effectively apply SXFM to practical experiments, it was improved to allow biologists and medical scientists to use it easily. We developed a practical version of SXFM by adding a sample changer, an optical differential interference contrast (DIC) microscope (NA = 0.25, Mag = ×10, reflection type), and a GUI-based software (Fig. 3.9). The sample changer consisting of a motorized θ stage and a multiple-sample holder can hold 12 samples, so that users can continuously observe samples for a long time without interruption caused by sample introduction. This also contributes to stable observation because the temperature is disturbed by sample introduction. The DIC microscope was placed just downstream of the sample without disturbing the X-ray path. It enables users to observe cells while measuring the distributions of elements with the SXFM. The software can control the sample changer and the DIC microscope, as well as the X-ray focusing system, the detector system, and the scanning stage. Users can easily measure the area they desire by making the corresponding rectangle on the DIC microscopic image in the software. Only the desired cells can be selected and effectively observed. In addition, it is important to maintain the temperature approximately constant (within

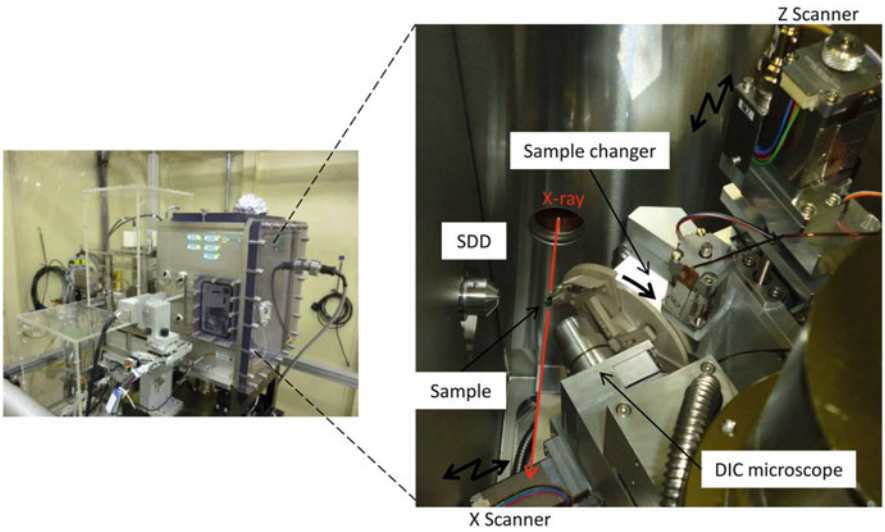

Fig. 3.9 Photograph of user-friendly SXFM. The whole system including the KB mirrors and the sample chamber (*left*) and inside the sample chamber (*right*)

~0.1 K) for user operation because beam broadening occurs upon a change in the temperature and readjustment of the focusing system is laborious. The room temperature control system consisting of platinum resistance temperature detectors and panel heaters was developed in collaboration with the optics group of the Japan Synchrotron Radiation Research Institute (JASRI). It is very suitable for KB mirror optics because it provides no vibration to the KB mirror system, which is sensitive to vibration. SXFM observation without adjustment of the focusing system could be performed over ~5 days.

3.3.2 Sample Preparation

The imaging of living cells without fixation and staining is the best way to observe their native state; however, living cells are not available for SXFM due to cell damage by the synchrotron X-rays via radicals. Fixation by washing and drying has often been applied for SXFM, but this alters the status of elements (Fig. 3.10). Free ions such as potassium and calcium were shown to be almost completely lost after fixation and washing, while zinc and copper were well maintained. These findings suggested that elements that bind strongly to cellular molecules are resistant to fixation and washing. These findings suggest the reliability of data for samples subjected to fixation and washing, as far as the data can be reproducibly obtained with appropriate controls, although we recommend freeze-drying or flash-freezing for SXFM (cryo-SXFM, Fig. 3.11), which are widely used to maintain the native

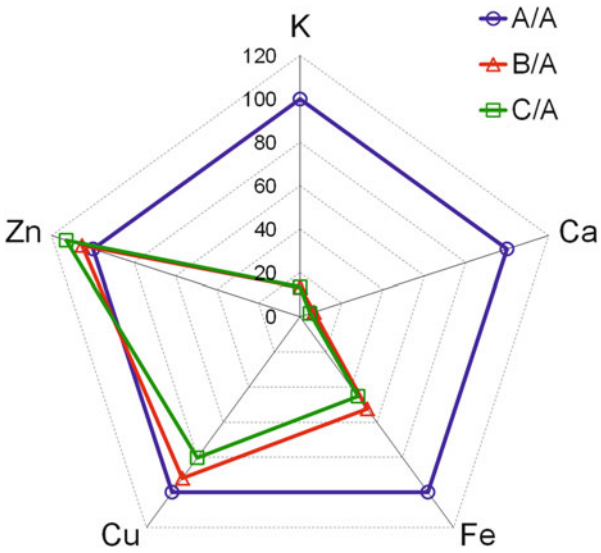

Fig. 3.10 Leakage of intracellular elements due to cell preparation. The intracellular potassium, calcium, and iron levels were markedly influenced by the cell preparation, whereas zinc and copper were unaffected. HeLa cells (10^7 cells) were centrifuged at 300 × g for 3 min (**Sample A**). The cells were then washed with phosphate-buffered saline (PBS) and fixed with 4 % paraformaldehyde in PBS for 10 min (**Sample B**). They were then permeabilized for 5 min with 0.2 % Triton X-100 in PBS and subsequently washed with PBS (**Sample C**). Average element levels (potassium, calcium, iron, copper, and zinc) of the samples A, B, and C were measured by inductively coupled plasma mass spectrometry (ICP-MS). The axis in the chart shows the ratios of B and C to A [18]

state in other forms of microscopy, such as electron microscopy, LA-ICP-MS, and NanoSIMS [17]. The fixation of clinical samples thus appears to be a practical approach.

3.3.3 Basement for Cells

Selecting a basement for cells is very important for imaging intracellular trace elements, since the basement influences the image background. We selected a commercially produced SiN basement. SiN has advantages in terms of its relative purity and thin layer (200 nm), which reduces elastic scattering. Its hydrophilicity also promotes cell adhesion and growth. In addition, the flatness of the membrane enables easy detection by DIC microscopy. On the other hand, SiN is associated with an intense silica peak, disturbing the detection of phosphorus and sulfur, which are essential for cellular function. We thus used a high-polymer membrane to avoid an intense Si peak as a background and applied carbon deposition to increase the hydrophilicity, resulting in sufficient cell growth (Fig. 3.12b). We call this

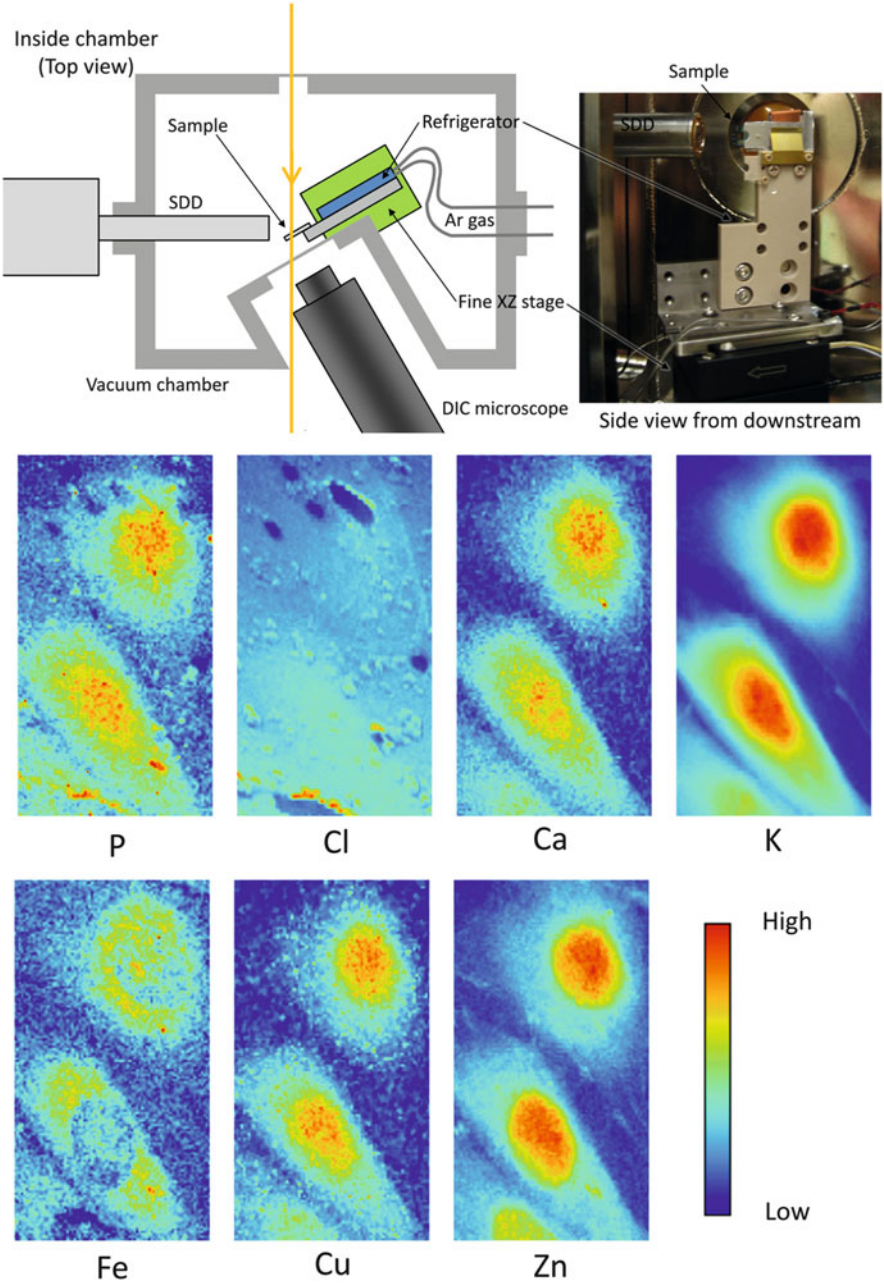

Fig. 3.11 Schematic and photograph of cryo-SXFM system (*upper*) and element mapping of frozen-hydrated cells (*lower*) (The figure is taken from Matsuyama et al. 2010, with permission [18])

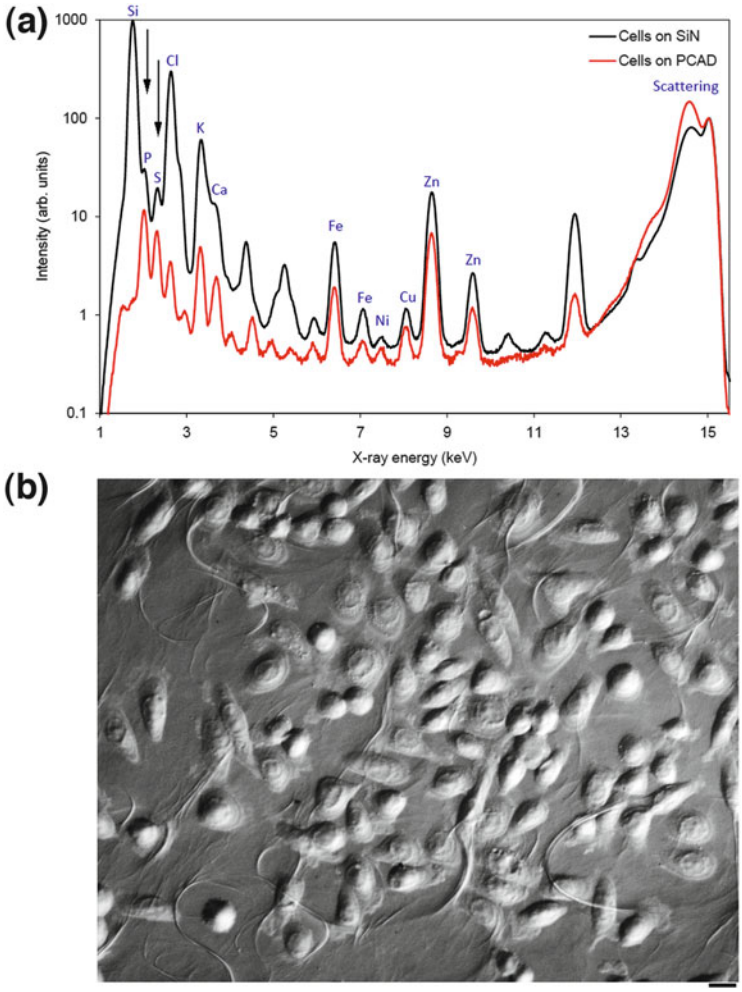

Fig. 3.12 PCAD basement. (**a**) Typical X-ray fluorescence spectra of cells on a SiN basement and polymer film with carbon deposition (PCAD) basement. *Arrows*, PCAD showed better peaks of phosphorus and sulfur than SiN. (**b**) Differential interference contrast (DIC) images of cells on a PCAD basement. Cells were well attached and growing. Scale bar, 10 μm (The figure is from Shimura and Matsuyama JSR 2010 via a copyright agreement)

membrane polymer film with carbon deposition (PCAD). PCAD allows the appearance of clear sulfur and phosphorus peaks and sufficient cellular adhesion (Fig. 3.12a).

3.3.4 Element Array

The system used for array analysis based on information on multiple elements from a single cell has been termed an element array [4]. For example, an element array can clarify the zinc dynamics of cells sensitive and resistant to anticancer drugs (Fig. 3.13). We also found that reduced glutathione was highly correlated with zinc regulation. Glutathione is a zinc-related protein that functions in excretion. We hypothesized that glutathione pumps out the drug in drug-resistant cells. In fact, a zinc-chelating agent combined with drug treatment for 5 consecutive days suppressed drug excretion and increased drug uptake and effects [4]. Array analysis thus suggested a new solution to drug resistance. High-resolution mapping images of the intracellular distribution are not always required for array analysis; however, array analysis is effective to evaluate the cell features with regard to the metallome and also in relation to cellular molecules.

3.3.5 A Cell Line Subjected to Sample Imaging at the Single-Cell Level

After a user-friendly version of SXFM was established, we could obtain more images at the single-cell level to reveal cellular function. Representative images obtained by SXFM are shown. Images of a 500-nm cryo-section of multiple myeloma (MM, blood cancer cell lines) were taken using the PCAD basement. The PCAD made it possible to image phosphorus clearly at the nucleus (Fig. 3.14), where there were some phosphorus-enriched regions. Zinc did not overlap with the phosphorus-enriched regions. In contrast, iron colocalized with the phosphorus-enriched regions, but showed a punctate distribution. These different localizations and patterns suggested that each element has different binding partners and roles. These elements may play roles in cancer cell proliferation. In further experiments, it may be possible to upregulate or suppress gene function to influence the localization of these elements. Information on the distribution of elements at the single-cell level has the potential to reveal novel nuclear functions.

3.3.6 Clinical Samples

Most clinical samples had already been fixed in formaldehyde solution at a pathology department. However, even fixed samples are informative if the data are reproducible and supported by control samples. We applied clinical samples to SXFM using cryo-sections (Fig. 3.15). Cryo-sections of bone marrow cells from MM cases and healthy volunteers were prepared by the Tokuyasu method, which is widely used for electron microscopy [19]. There was greater accumulation of

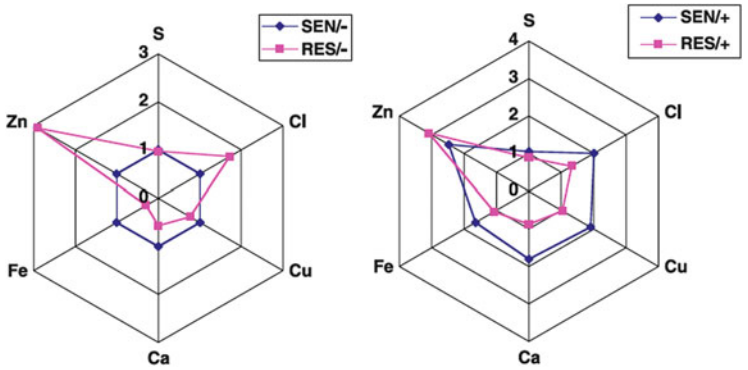

Fig. 3.13 Element array analysis based on mapping data from SXFM. The mean signal intensity of each element obtained by SXFM was calculated, and the fold increase of elements in drug-resistant (RES) cells is depicted using the mean signal intensity in drug-sensitive (SEN) cells as a standard (*left*). SEN and RES cells were treated with (+) or without (−) 1 μM cisplatin, a platinum-based anticancer drug. Notably, the fold increase of zinc in RES cells was greater than that in SEN cells without treatment (*left*, *red framed*). The fold increase of zinc in SEN cells was increased by cisplatin uptake, while the level in RES cells was stable (*right*). *SEN* cisplatin-sensitive cells, *RES* cisplatin-resistant cells, *S* sulfur signal, *Zn* zinc signal, *Fe* iron signal, *Ca* calcium signal, *Cu* copper signal, and *Cl* chlorine signal (The figure is taken from Shimura et al. 2005 [4])

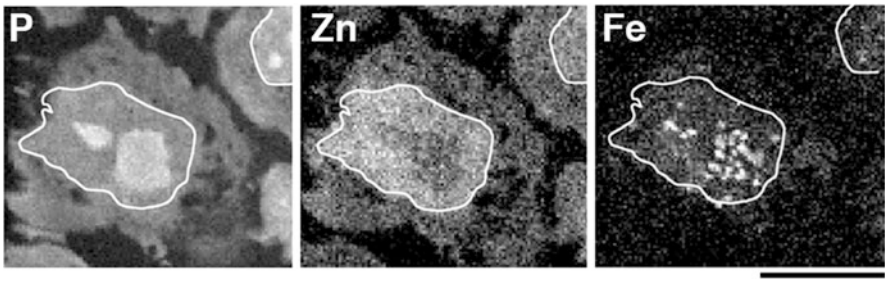

Fig. 3.14 Images of intracellular phosphorus, zinc, and iron mapping using a multiple myeloma (MM) cell line. Cryo-sections (500 nm thick) of cells were imaged with the following parameters: exposure = 1 s/pixel, scanning step = 250 nm/pixel, and X-ray energy = 15 keV. Bar, 10 μm. A *white* border indicates the nucleus (The figure is from Shimura and Matsuyama JSR 2010 via a copyright agreement)

copper and zinc in the MM cytoplasm than in that of healthy volunteers. There was also marked accumulation of nickel in MM bone marrow cells, compared with that in healthy volunteers, which we had not observed in the MM cell line (Fig. 3.14). Nickel was well detected in MM patient serum and was suspected of being a contaminant due to environmental pollution [20], although the mechanism by which it exerts carcinogenic effects is still unknown. Our imaging data suggested that nickel influences bone marrow cells. In fact, cancer was thought to emerge at bone marrow cells during the process of cell maturation [21]. Since nickel induced

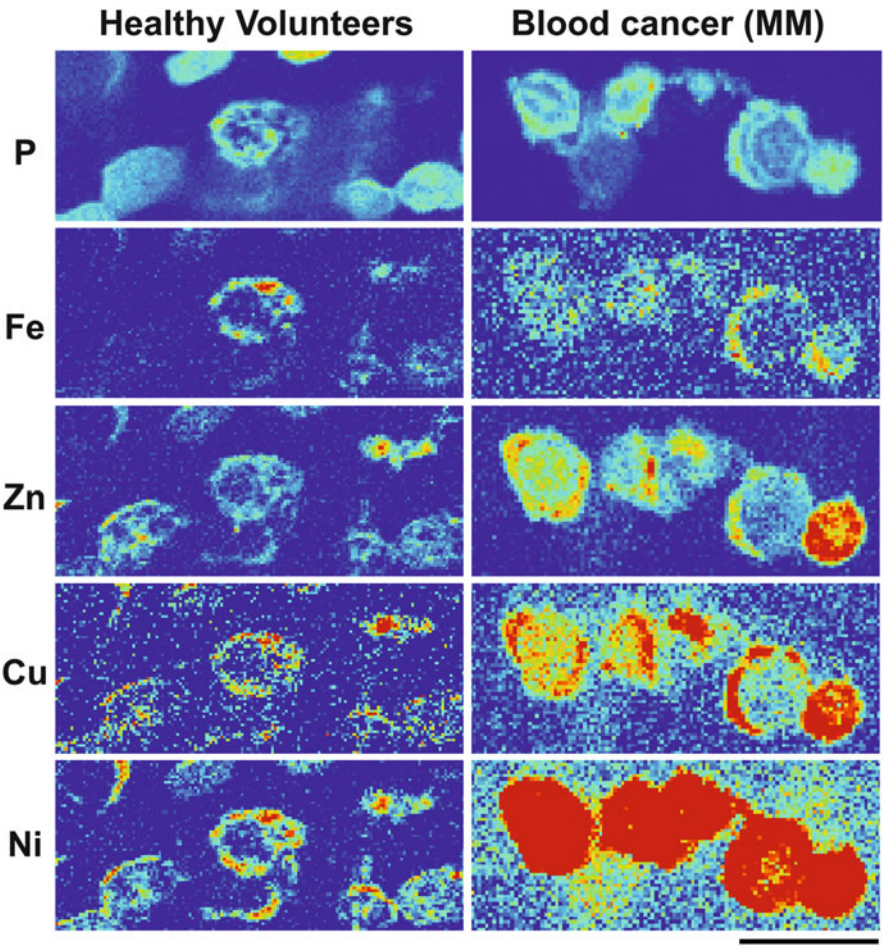

Fig. 3.15 Images of intracellular phosphorus, iron, zinc, copper, and nickel mapping in bone marrow cells derived from a clinical case of MM (*right*) and healthy volunteers (*left*). Cryosections (3 μm) of each sample were taken using the following parameters: exposure = 1 s/pixel, scanning step = 600 nm/pixel, and X-ray energy = 15 keV. Bar, 10 μm. Samples were obtained after approval from the Committee of the NCGM (#NCGM-G-00623-02), in accordance with the Declaration of Helsinki

DNA damage [22] (see also the metal targeting system in the next section), we cannot rule out the possibility of a relationship between nickel contamination and MM. Our data suggest that the clinical sample reflected the background of the donor, such as their living environment and diet, in the past and present, which is distinct from culture cells in the laboratory. Element imaging in clinical samples may thus shed light on the etiology and pathology and might contribute to diagnosis and prognosis in future medical applications.

3.3.7 Application in Metal Transport with Targeting

Previous findings suggested that the carcinogenic activity of Ni^{2+} depends on how this ion enters the cell and reaches the chromatin in the nucleus [23]. As the intracellular location of Ni^{2+} is related to cytotoxicity [24], genotoxicity [22], and the induction of oxidative stress [25], it would be desirable to characterize such effects in relation to intracellular metal localization. To understand the effects and cytotoxicity of metals in each part of the cell, it is necessary to have appropriate technology in terms of both the targeting system and the imaging for localization at the single-cell level. For this purpose, we applied our new metal transport system combined with SXFM.

3.3.8 Transporter

Our main goal for targeting metal transporters was to introduce metal ions (Ni^{2+}) at the selected cellular organelle without altering their natural activity. Such ions are delivered to the target organ and then released by a transporter (Fig. 3.16a). Note that the process of metal dissociation from a transporter differs from that for probes with a radionuclide semi-covalently bound to the chelators. In contrast, metals may be located diffusely or absorbed by membranes, for example, in the endoplasmic reticulum or mitochondria, or accumulate due to endocytosis by natural pathways (Fig. 3.16b). Two major conditions were taken into account for designing transporters. First, they should have a selective targeting domain. Ideal candidates have to show high specificity for the targeted organ, such as transactivator of transcription (TAT) (see the section on cell-penetrating peptides). Second, the metal-binding domain has to be constructed carefully, as metal-binding affinity is adjusted to hold the metal during transport, but not to chelate the metal completely so that it can be released at the cellular target. Metal dissociation may be controlled by different processes, for example, by changes in the redox potential at the organelle, different levels of intracellular ligands, which may compete with the transporter in metal binding, or transporter proteolysis, which potentially influences the metal-binding stability. Other issues also have to be taken into account, such as the cellular response or chemical kinetic features of metal ion binding. Stabilization of metal ion binding with various modifications in the structure of the three arms of 2,3-diaminopropionic acid (Dap)-branched peptides and the increased cell penetration and improved selectivity properties of branched "shuttles" are good candidates for such transporting platforms.

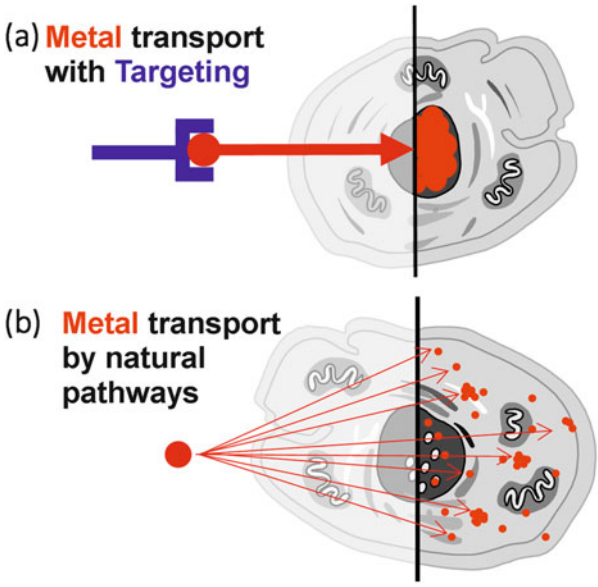

Fig. 3.16 Schematic presentation of metal transport with targeting (**a**) in contrast to metal transport via natural pathways (**b**)

3.3.9 Cell-Penetrating Peptides (CPPs)

The application of CPPs for targeting organelles is a well-known approach [26]. Such peptides are usually developed based on the natural sequences of proteins or synthetically developed sequences. They are applied to the transfer of nucleotides [27, 28], small molecules [26, 29], and tightly bound metal chelator radionuclides [30, 31] in both in vitro and in vivo systems. One of the most common applications of CPPs is as peptides from the TAT protein of the human immunodeficiency virus [32]. Recent developments in peptide branching have allowed us to increase their penetration properties [33], which enhance multiple effects associated with cell uptake [34]. Moreover, branching with Dap can stabilize metal ion-binding activity in monomeric complexes [35, 36]. It was shown that CPP branching increased the permeation [37] and molecular recognition of biomolecules [38]. The TAT fragments were shown to be compatible for branching to increase cell targeting. This potential to exhibit a targeting function when in branched structures has been reported in the literature. We chose the fragment $TAT_{47–57}$ to design an artificial Ni^{2+}-branched peptide transporter by adding the Dap residue to the N-terminal. This allows further extension of peptide N-terminals with histidine donors to create a metal-binding junction. Finally, the H-HisDap (H-His)-Tyr^{47}-Gly-Arg-Lys-Lys-Arg-Arg-Gln-Arg-Arg-Arg-OH(A) peptide was synthesized (Fig. 3.17). An electrospray ionization MS study indicated that nickel is bound in an equimolar complex, and hot electron capture dissociation (HECD) MS fragmentation data indicate that nickel is bound in the designed fork (Fig. 3.17). To obtain information on metal-binding affinity, we performed

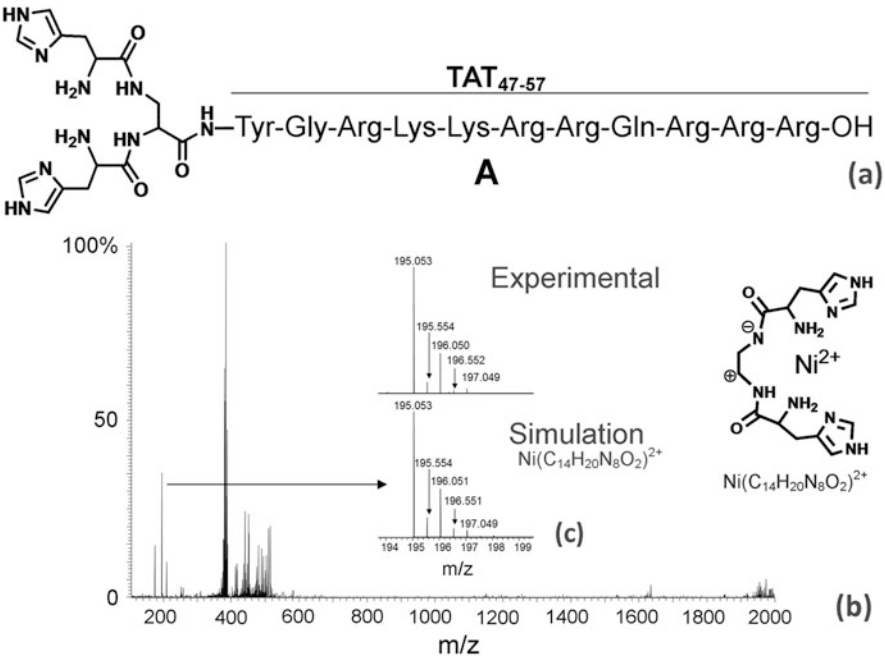

Fig. 3.17 The electrospray ionization dual MS (ESI-MS/MS) measurements were performed using an Orbitrap Velos mass spectrometer in positive ion full scan mode. The concentration and molecular ratio of apopeptide A were 6×10^{-5} M and 1 Ni:1 A, respectively. (**a**) Structure of the branched peptide. (**b**) The higher-energy collision dissociation spectra. (**c**) The signal corresponding to the $Ni(C_{14}H_{20}N_8O_2)^{2+}$ species. Data acquisition and treatment were performed using Xcalibur 2.1 software (The figure is taken from Szyrwiel et al. [5])

potentiometric experiments with the fragment responsible for metal ions binding H-His-Dap-(H-His)-Tyr-NH_2. Potentiometric studies have indicated that Ni^{2+} ions bind with $pNi^{2+} = 5.9$ at physiological pH (where $pNi^{2+} = -\log[Ni^{2+}_{frre}]$)[5]. Our transport with a targeting system allowed Ni^{2+} transport into the nucleus, which was imaged by SXFM (Fig. 3.18, NiA) [5]. On the other hand, effective metal uptake above the background level was not seen in the cells treated with an equivalent number of moles of nickel ions. The level of nickel-induced DNA damage was ten times greater for NiA than for nickel ions (Fig. 3.19). These findings imply that our transport actually moved nickel ions into the nucleus and induced DNA damage [5].

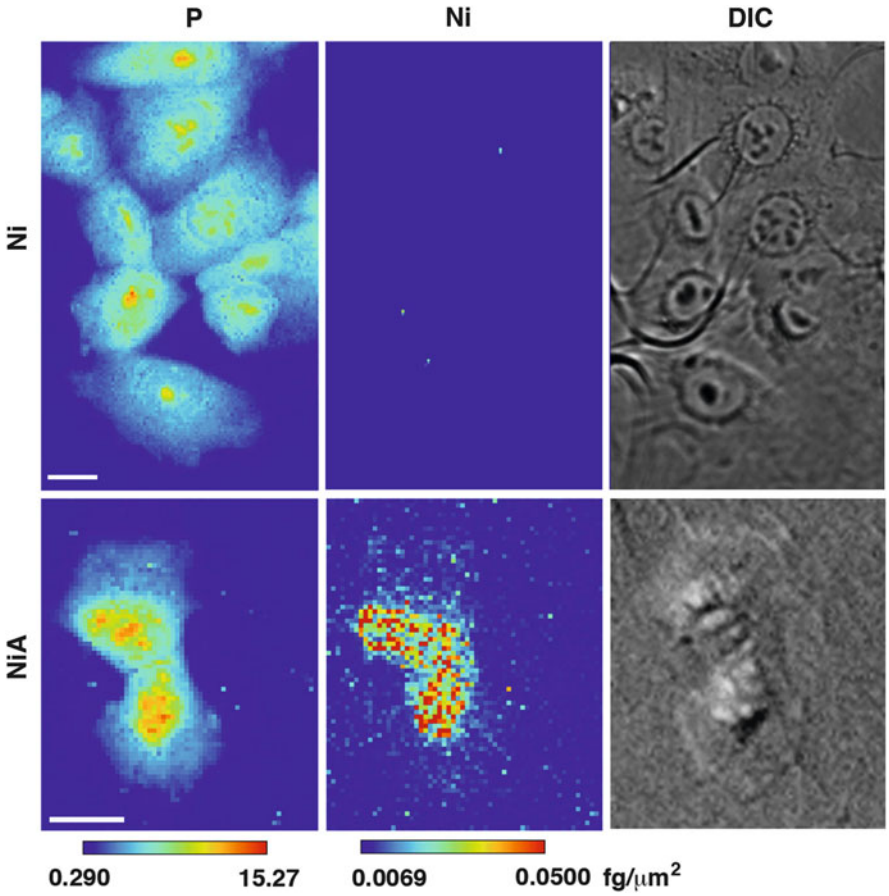

Fig. 3.18 Images of intracellular nickel mapping in cells treated with Ni or NiA. Cells were treated with Ni ion (*top*) or NiA (*bottom*) for 20 min. DIC, differential interference contrast images. A brighter color indicates higher signal intensity. Color bar, fg/μm^2; bar, 10 μm (The figure is taken from Szyrwiel et al. 2015 [5])

3.4 Future SXFM

3.4.1 Improvement of X-Ray Sources

Innovative X-ray sources suitable for X-ray nano-spectroscopy including SXFM are now strongly anticipated. One of them is the diffraction-limited storage ring (DLSR), using an ultralow-emittance storage ring with an undulator [39]. It is capable of generating a small and intense X-ray source leading to the formation of a very intense nanobeam with focusing optics. As mentioned above, the current SR X-ray source is much larger than that required to focus X-rays down to a few

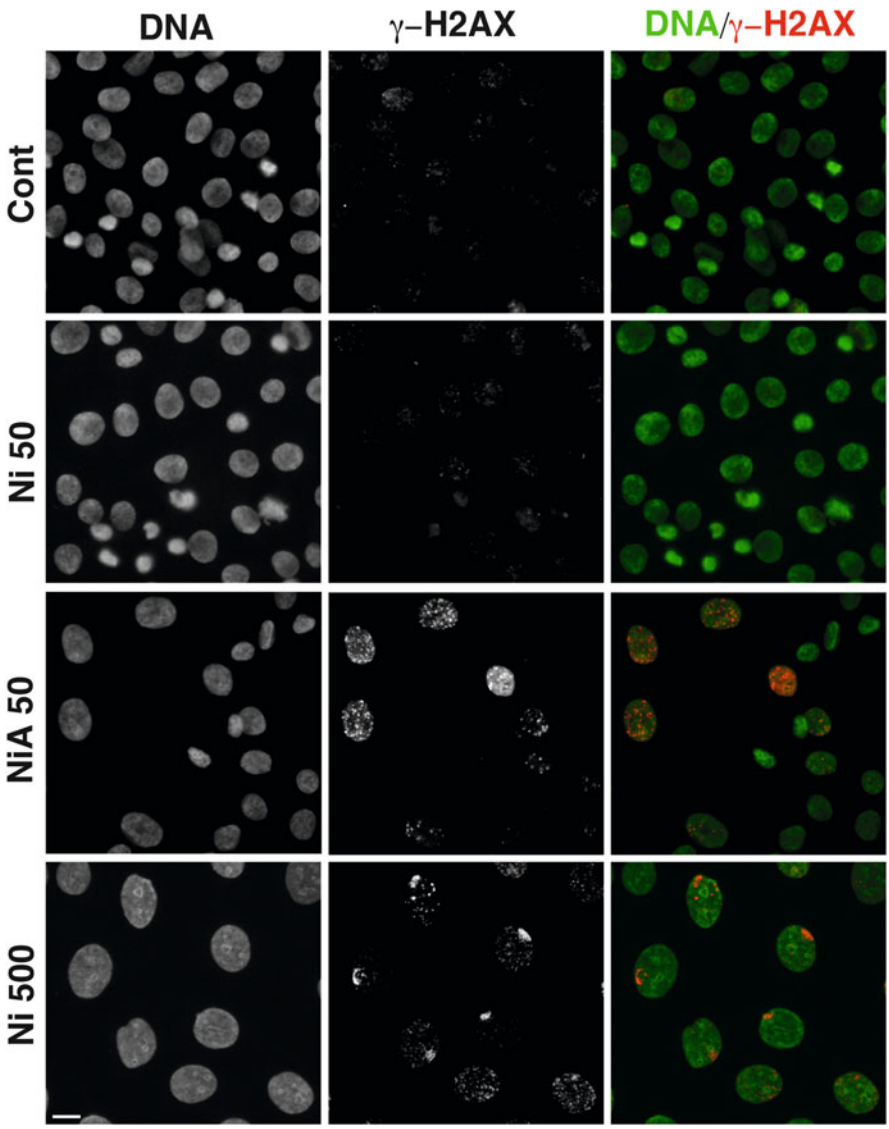

Fig. 3.19 DNA damage in NiA- and Ni ion-treated cells. DNA damage was estimated based on focus formation by immunostaining with an anti-γ-H2AX antibody. Note that NiA50 cells showed more significant focus formation (DNA damage) than Ni50 cells (*second* and *third panels*). Cont, untreated control cells; Ni50, cells treated with 50 μM Ni ions; NiA50, cells treated with 50 μM NiA for 48 h; and Ni500, cells treated with 500 μM Ni ions (The figure is taken from Szyrwiel et al. 2015 [5])

tens of nanometers without loss of the generated X-rays. Therefore, we have to reluctantly block X-rays with a slit near the light source. However, if DLSRs become available, it will be possible to collect almost all X-rays at the focus with existing focusing optics. A paper introducing the DLSR of SPring-8 [40] describes that very intense nanobeams with photon flux of ~10^{14} photons/s and beam size of 230 (H) nm × 120 (V) nm can be achieved with existing techniques. This is ~1000 times as many photons as our formed nanobeam. SXFM with both high resolution and high sensitivity will enable the detection of trace elements present at very low levels in a single mitochondrion within a short time. Fortunately, plans to construct DLSRs are being implemented all over the world, such as NSLS-II in the USA (started operation in 2015), MAX IV in Sweden, Sirius in Brazil, ESRF Upgrade in France, SPring-8 II in Japan, and APS Upgrade in the USA. The development of beamline optics, focusing optics, and X-ray microscopes has also been initiated, with the aim of realizing optics and systems specialized for the new X-ray sources.

3.4.2 High-Resolution SXFM

The current goal in developing scanning-type X-ray microscopes including SXFM is to achieve high resolution better than 10 nm. Possible techniques to achieve this are the multilayer Laue lens (MLL) [41] and the multilayer focusing mirror [42, 43] (Fig. 3.20a, b). An MLL, which is a kind of diffraction lens, can overcome the difficulty in fabricating diffraction lenses, in that the fabrication of very fine and thick patterns with a minimum period of less than 10 nm and device thickness of larger than a few microns is very challenging. An MLL fabricated with a magnetron sputtering deposition technique could focus 12-keV X-rays to an 11.2-nm (full width at half maximum, FWHM) spot with 15 % efficiency [41]. In addition, a multilayer focusing mirror can overcome the limitation that the grazing-incidence angle, proportional to the numerical aperture, of a total-reflection focusing mirror cannot be increased. Multilayer focusing mirrors can reflect and focus X-rays by using Bragg reflection, even when the grazing-incidence angle is large, leading to a very small focus size. FWHM of 7 nm has now been achieved using a multilayer KB system consisting of two multilayer focusing mirrors at X-ray energy of 20 keV (Fig. 3.21) [42, 43]. However, because there are no MLLs and multilayer mirrors to completely satisfy the requirements of spectroscopy users with regard to throughput, stability, and so on, few practical experiments have been implemented. Future improvements together with DLSR developments are anticipated. In the text below, other possible upgrades are briefly described. For more detail, please see the corresponding references, **deformable mirror** [44]. A deformable mirror (Fig. 3.22a) is a very powerful tool to change the optical system adaptively and moreover to directly compensate for wave front errors. For example, we can change the focal length depending on the experiment, the sample size, and the temporary apparatus used, such as a cooler or a heater. We can also produce an ideally focused beam even when wave front aberration is caused by beamline optics, such as a

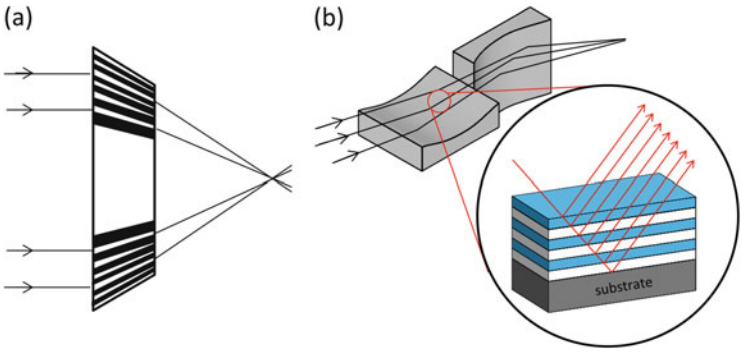

Fig. 3.20 High-resolution focusing optics. (**a**) Multilayer Laue lens. (**b**) Multilayer Kirkpatrick-Baez mirrors

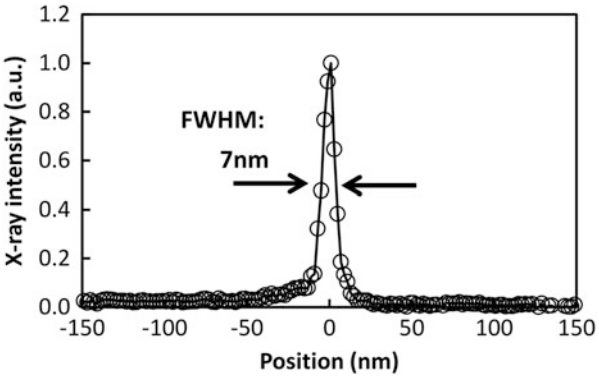

Fig. 3.21 X-ray focused beam with full width at half maximum of 7 nm (The figure is taken from Yamauchi et al. 2011, with permission [43])

monochromator, mirrors, or a vacuum window. Very precise adaptive mirrors and related techniques have been successfully developed, **ellipsoidal mirror** [45]. An ellipsoidal mirror (Fig. 3.22b) can produce a two-dimensional focusing beam with a single mirror, unlike KB mirror optics consisting of two mirrors. It has many advantages with regard to focusing efficiency, simple alignment, and stability of the focusing beam size and position because of the reduction in the number of mirrors. However, the fabrication process is very difficult because the shape involves a radius of curvature of a few millimeters in the short axis direction. Substantial efforts have been made to develop ultraprecise machining and measurement methods, **imaging mirror as focusing optics** [46]. SXFM usually uses focusing mirror optics such as KB mirrors, not imaging mirror optics such as advanced KB mirrors (Fig. 3.22c) and Wolter mirrors. Although KB mirror optics can focus X-rays, it cannot form clear images because it suffers from fatal comatic aberration leading to an unclear image, except in the central region. If imaging

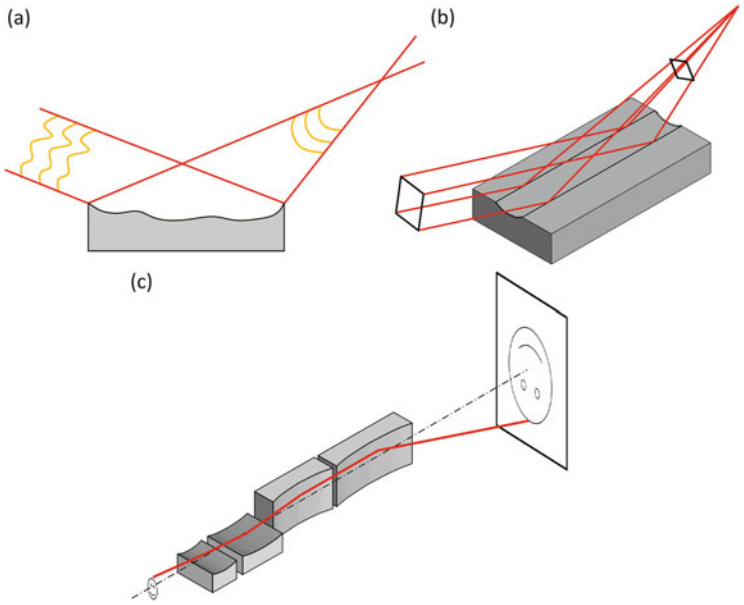

Fig. 3.22 Advanced focusing optics. (**a**) Deformable mirror. (**b**) Ellipsoidal mirror. (**c**) Advanced Kirkpatrick-Baez mirrors

mirror optics at the demagnification geometry is used, X-rays can invariably be focused even when the mirror inclines due to thermal drift or misalignment. This is because imaging mirrors can focus X-rays at off-axis conditions as well as at on-axis ones. Valuable beam time at the SR facilities can thus be saved by reducing the adjustment time for focusing optics of SXFM.

3.4.3 Possible Labeled Probes

Single-element labeling combined with SXFM may allow the imaging of nucleotides, proteins, secondary antibodies, and synthetic biomolecules, such as metabolites, transmitters, or organic drugs. In fact, SXFM successfully imaged a mitochondrion, an organelle with a diameter of less than 1 μm, using a metal-conjugated secondary antibody, as well as fluorescence imaging (Fig. 3.8). Data also suggested the possibility of linking SXFM to other -omics, such as metallomics, metabolomics, genomics, and proteomics (Fig. 3.23). Intracellular small molecules, such as fatty acids, sugars, and their derivatives, which are difficult to label for imaging due to their structural alterations, might be among the candidates for imaging using SXFM. If a single element is used to label these molecules at appropriate positions, SXFM has the potential to reveal their intracellular location during their metabolism. In Fig. 3.24a, elements suitable for the

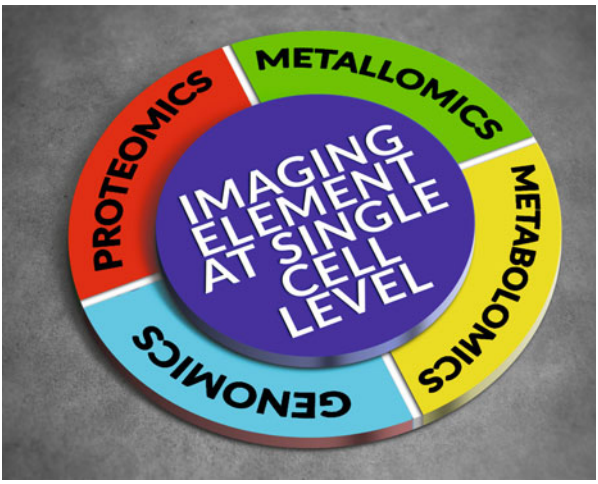

Fig. 3.23 The linkage between imaging elements (biomolecules) at the single-cell level and other -omics fields

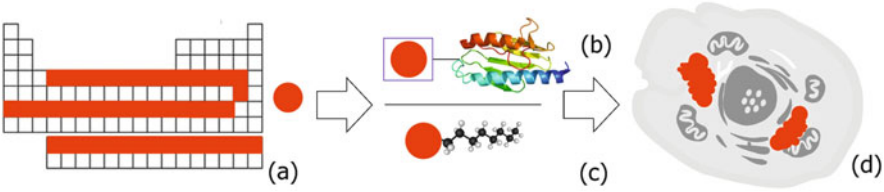

Fig. 3.24 Schematic presentation of biomolecules labeled with chemical elements for SXFM: (**a**) Chemical elements detectable by the current SXFM are indicated in *red*. (**b**) Labeling biomolecules with binding groups or nanoparticles attached to high-molecular-weight molecules. (**c**) Biomolecules directly labeled with elements for low-molecular-weight molecules. (**d**) Imaging of intracellular elements used to label biomolecules by SXFM

current SXFM are marked in red. It is notable that many elements are available for labeling molecules for detection by SXFM; however, major criteria for selecting elements for labeling depend on the actual cell status, as follows: (1) The signal intensity of the element label has to be higher than the cellular background level, for example, cells have a high level of zinc in the nucleus, so zinc labeling is not suitable for nuclear detection by SXFM. (2) The labeled probe with elements also has to exhibit thermodynamic and chemical stability to avoid intracellular exchange with cell components; consideration of the intracellular thiol compounds is particularly necessary. (3) Finally, it is also necessary for the labeled compound not to alter biological functions. Labeling biomolecules are mainly categorized as follows: (i) those with binding groups or nanoparticles attached to high-molecular-weight molecules (Fig. 3.24b) and (ii) biomolecules directly labeled with elements for low-molecular-weight molecules (Fig. 3.24c). If the element labels the complex

appropriately, SXFM has the potential to reveal its intracellular location (Fig. 3.24d).

3.4.4 Application of Medical Probes to SXFM

Potential SXFM probes are suitable for other medical imaging methodologies, such as positron emission tomography, single-photon emission computed tomography, computer tomography, and magnetic resonance imaging. By introducing an element suitable for selected methodologies, such as gadolinium or bromine, into their structure, compounds can be observed within the entire body by medical imaging and within the cell by SXFM upon a biopsy. Moreover, cellular imaging of labeled drugs or radiopharmaceuticals at the micro-organelle level could reveal their uptake status and the processes affecting them in vitro, which would be interesting for elements such as gadolinium, bromine, technetium, and other reference isotopes for contrast media. This technology may open up new opportunities and challenges for the application of SXFM, improving our knowledge of cellular functions and disease processes, as well as helping in new drug development.

3.4.5 SXFM Application for Different Types of Microscopy

To understand cellular functions, a range of information, such as on cellular morphology, element distribution, protein distribution, and other cell biological and biochemical quantitative parameters, has to be collated. In particular, it is useful to combine information from multiple images collected from the same cell using various microscopes. As mentioned above, labeling proteins of interest with a metal or a fluorescent dye and observing them using a visible-light fluorescence microscope and SXFM is one possible approach (Fig. 3.8). It may be possible to link the obtained information with other -omics, for example, metallomics, metabolomics, genomics, and proteomics (Fig. 3.23). Moreover, the addition of electron microscopic data is very helpful to understand the relationship between ultrafine structures and the distributions of elements. X-ray absorption fine structure (XAFS) analysis in combination with a scanning technique, XAFS imaging, is also compatible with SXFM.

3.5 Collaboration on Platforms in Different Fields

Platforms based on many fields, such as biology, medicine, chemistry, engineering, and physics, are essential for innovative studies and the future development of element imaging at the single-cell level (Fig. 3.25). Element imaging at the single-

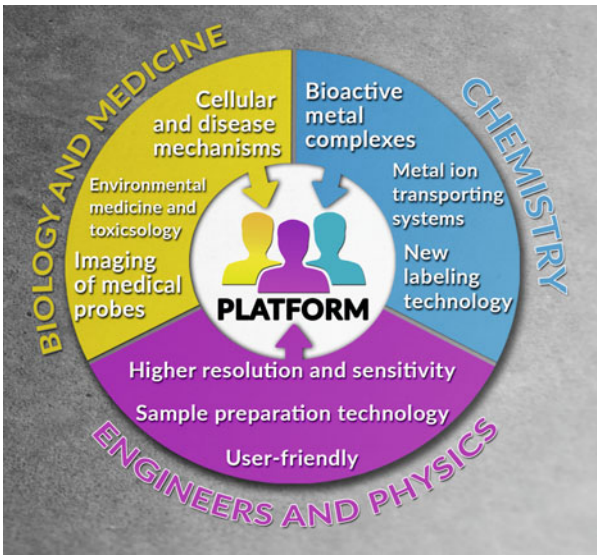

Fig. 3.25 A platform based on many fields, such as biology, medicine, chemistry, engineering, and physics, for innovative studies and future development of imaging at the single-cell level

cell level is beneficial for studies in biology and basic medicine by enabling the exploration of general cellular function and disease mechanisms. It is also important to apply such imaging to clinical samples that are expected to be affected by environmental pollution, diet, and toxicology, but for which it is difficult to draw definitive conclusions by conventional medical laboratory tests. Additionally, element imaging at the single-cell level can be applied to imaging drugs, contrast media, and radiopharmaceuticals labeled with elements. In the field of chemistry, a new technology of labeling molecules with elements should lead to the development of multiple new applications. Chemists may also propose new bioactive metal complexes and metal-ion-transporting systems. Moreover, collaboration among physicists, engineers, biologists, and chemists should enhance the development of other physicochemical methodologies that focus on intracellular elements, such as Q-dot [47], and should improve detection limits and sensitivity, including sample preparation technology, and be user-friendly. Collaboration among different fields may also lead to the imaging of other organisms such as viruses that are less than 100 nm in size at the electron microscopic level. While this may produce novel insights and products in various fields, integration of knowledge arising in diverse fields may initially be challenging.

3.6 Conclusion

The SXFM system described in this paper can reliably determine the cellular distribution of multiple elements using a sub-100-nm focusing approach. Labeling with a single element and imaging by SXFM should contribute to the understanding

of interactions among intracellular elements (the metallome) and other biological molecules such as proteins, nucleic acids, lipids, and sugars (the other -omics). Future advanced mirror systems and more intense photon beams at synchrotron facilities should enable us to obtain higher-resolution images at higher speed than in current imaging. Visualizing intracellular elements at the single-cell level may provide great insights into the effects of such elements on cellular dynamics.

Acknowledgment We would like to thank Tetsuya Ishikawa at RIKEN for providing advice and encouragement during this study. We also acknowledge the help of Akihiro Matsunaga at the NCGM for the measurements and analyses of images, Shotaro Hagiwara at the NCGM hospital for clinical studies, and Yoshinori Nishino at Hokkaido University and Yoshiki Kohmura at RIKEN for assistance with the beamline adjustment. This study was supported by CREST from the Japan Science and Technology Agency (MS, SM, LS); MS was supported by a Grant-in-Aid for Research on Advanced Medical Technology, Ministry of Health, and Labor and Welfare of Japan; LS was supported by a Marie Curie Intra-European Fellowship from the European Union (PIEF-GA-2012-329969).

References

1. Crone B, Aschner M, Schwerdtle T et al (2015) Elemental bioimaging of Cisplatin in Caenorhabditis elegans by LA-ICP-MS. Metallomics 7(7):1189–1195
2. Godinho RM, Cabrita MT, Alves LC et al (2014) Imaging of intracellular metal partitioning in marine diatoms exposed to metal pollution: consequences to cellular toxicity and metal fate in the environment. Metallomics 6(9):1626–1631
3. Thompson CM, Seiter J, Chappell MA et al (2015) Synchrotron-based imaging of chromium and gamma-H2AX immunostaining in the duodenum following repeated exposure to Cr(VI) in drinking water. Toxicol Sci 143(1):16–25
4. Shimura M, Saito A, Matsuyama S et al (2005) Element array by scanning X-ray fluorescence microscopy after cis-diamminedichloro-platinum(II) treatment. Cancer Res 65(12):4998–5002
5. Szyrwiel L, Shimura M, Shirataki J et al (2015) A novel branched TAT(47–57) peptide for selective Ni(2+) introduction into the human fibrosarcoma cell nucleus. Metallomics 7 (7):1155–1162
6. Blackiston DJ, McLaughlin KA, Levin M (2009) Bioelectric controls of cell proliferation: ion channels, membrane voltage and the cell cycle. Cell Cycle 8(21):3527–3536
7. Zhang J, Wei J, He Q et al (2015) SKF95365 induces apoptosis and cell-cycle arrest by disturbing oncogenic Ca(2+) signaling in nasopharyngeal carcinoma cells. Onco Targets Ther 8:3123–3133
8. Jourdan E, Marie Jeanne R, Regine S et al (2004) Zinc-metallothionein genoprotective effect is independent of the glutathione depletion in HaCaT keratinocytes after solar light irradiation. J Cell Biochem 92(3):631–640
9. Klug A (2010) The discovery of zinc fingers and their development for practical applications in gene regulation and genome manipulation. Q Rev Biophys 43(1):1–21
10. Mantler M, Schreiner M (2000) X-ray fluorescence spectrometry in art and archaeology. X-Ray Spectrom 29(1):3–17
11. Tanaka T SPECTRA synchrotron radiation calculation code. SPring-8 Center, Hyogo, pp 679–5148. http://radiant.harima.riken.go.jp/spectra/index.html
12. Matsuyama S, Mimura H, Yumoto H et al (2006) Development of scanning x-ray fluorescence microscope with spatial resolution of 30nm using Kirkpatrick-Baez mirror optics. Rev Sci Instrum 77(10):103102

13. Yamauchi K, Mimura H, Inagaki K et al (2002) Figuring with subnanometer-level accuracy by numerically controlled elastic emission machining. Rev Sci Instrum 73(11):4028–4033
14. Matsuyama S, Mimura H, Yumoto H et al (2006) Development of mirror manipulator for hard-x-ray nanofocusing at sub-50-nm level. Rev Sci Instrum 77(9):093107
15. Matsuyama S, Shimura M, Mirnura H et al (2009) Trace element mapping of a single cell using a hard x-ray nanobeam focused by a Kirkpatrick-Baez mirror system. X-Ray Spectrom 38 (2):89–94
16. Matsuyama S, Mimura H, Katagishi K et al (2008) Trace element mapping using a high-resolution scanning X-ray fluorescence microscope equipped with a Kirkpatrick-Baez mirror system. Surf Interface Anal 40(6–7):1042–1045
17. Walther P, Studer D, McDonald K (2007) High pressure freezing tutorial. Microsc Microanal 13(S02):440–441
18. Matsuyama S, Shimura M, Fujii M et al (2010) Elemental mapping of frozen-hydrated cells with cryo-scanning X-ray fluorescence microscopy. X-Ray Spectrom 39(4):260–266
19. Griffiths G, SLOT JW, Webster P (2015) Kiyoteru Tokuyasu: a pioneer of cryo-ultramicrotomy. J Microsc 260(3):235–237
20. Egedahl R, Coppock E, Homik R (1991) Mortality experience at a hydrometallurgical nickel refinery in Fort Saskatchewan, Alberta between 1954 and 1984. Occup Med 41(1):29–33
21. Gentry SN, Jackson TL (2013) A mathematical model of cancer stem cell driven tumor initiation: implications of niche size and loss of homeostatic regulatory mechanisms. PLoS One 8:e71128
22. Cameron KS, Buchner V, Tchounwou PB (2011) Exploring the molecular mechanisms of nickel-induced genotoxicity and carcinogenicity: a literature review. Rev Environ Health 26 (2):81–92
23. Costa M, Klein CB (1999) Nickel carcinogenesis, mutation, epigenetics, or selection. Environ Health Perspect 107(9):A438
24. Salnikow K, Kasprzak KS (2007) In: Sigel A, Sigel H, Sigel RK (eds) Nickel and its surprising impact in nature: metal ions in life sciences, vol 2. Wiley, Chichester, pp 581–618
25. Das KK, Büchner V (2007) Effect of nickel exposure on peripheral tissues: role of oxidative stress in toxicity and possible protection by ascorbic acid. Rev Environ Health 22(2):157–173
26. Milletti F (2012) Cell-penetrating peptides: classes, origin, and current landscape. Drug Discov Today 17(15):850–860
27. Welser K, Campbell F, Kudsiova L et al (2012) Gene delivery using ternary lipopolyplexes incorporating branched cationic peptides: the role of peptide sequence and branching. Mol Pharm 10(1):127–141
28. Liu Y, Kim YJ, Ji M et al (2014) Enhancing gene delivery of adeno-associated viruses by cell-permeable peptides. Mol Ther Methods Clin Dev 1:1–12
29. Sakhrani NM, Padh H (2013) Organelle targeting: third level of drug targeting. Drug Des Dev Ther 7:585
30. Polyakov V, Sharma V, Dahlheimer JL et al (2000) Novel Tat-peptide chelates for direct transduction of technetium-99m and rhenium into human cells for imaging and radiotherapy. Bioconjug Chem 11(6):762–771
31. Bullok KE, Dyszlewski M, Prior JL et al (2002) Characterization of novel Histidine-tagged tat-peptide complexes dual-labeled with 99mTc-tricarbonyl and fluorescein for scintigraphy and fluorescence microscopy. Bioconjug Chem 13(6):1226–1237
32. Zhao M, Weissleder R (2004) Intracellular cargo delivery using tat peptide and derivatives. Med Res Rev 24(1):1–12
33. Eggimann GA, Blattes E, Buschor S et al (2014) Designed cell penetrating peptide dendrimers efficiently internalize cargo into cells. Chem Commun 50(55):7254–7257
34. Eggimann GA, Buschor S, Darbre T et al (2013) Convergent synthesis and cellular uptake of multivalent cell penetrating peptides derived from Tat, Antp, pVEC, TP10 and SAP. Org Biomol Chem 11(39):6717–6733

35. Szyrwiel Ł, Szczukowski Ł, Pap JS et al (2014) The Cu2+ binding properties of branched peptides based on l-2, 3-diaminopropionic acid. Inorg Chem 53(15):7951–7959
36. Szyrwiel Ł, Pap JS, Szczukowski Ł et al (2015) Branched peptide with three histidines for the promotion of Cu II binding in a wide pH range–complementary potentiometric, spectroscopic and electrochemical studies. RSC Adv 5(70):56922–56931
37. AbrreyáMonreal I (2015) Branched dimerization of Tat peptide improves permeability to HeLa and hippocampal neuronal cells. Chem Commun 51(25):5463–5466
38. Wynn JE, Santos WL (2015) HIV-1 drug discovery: targeting folded RNA structures with branched peptides. Org Biomol Chem 13(21):5848–5858
39. Eriksson M, van der Veen JF, Quitmann C (2014) Diffraction-limited storage rings-a window to the science of tomorrow. J Synchrotron Radiat 21(5):837–842
40. Yabashi M, Tono K, Mimura H et al (2014) Optics for coherent X-ray applications. J Synchrotron Radiat 21(5):976–985
41. Huang X, Yan H, Nazaretski E et al (2013) 11 nm hard X-ray focus from a large-aperture multilayer Laue lens. Sci Rep 3:3562
42. Mimura H, Handa S, Kimura T et al (2010) Breaking the 10 nm barrier in hard-X-ray focusing. Nat Phys 6(2):122–125
43. Yamauchi K, Mimura H, Kimura T et al (2011) Single-nanometer focusing of hard x-rays by Kirkpatrick–Baez mirrors. J Phys Condens Matter 23(39):394206
44. Goto T, Nakamori H, Kimura T et al (2015) Hard X-ray nanofocusing using adaptive focusing optics based on piezoelectric deformable mirrors. Rev Sci Instrum 86(4):043102
45. Hirokatsu Y, Takahisa K, Satoshi M, Kazuto Y, Haruhiko O (2016) Stitching interferometry for ellipsoidal x-ray mirrors. Rev Sci Instrum 87:051905
46. Matsuyama S, Kidani N, Mimura H et al (2012) Hard-X-ray imaging optics based on four aspherical mirrors with 50 nm resolution. Opt Express 20(9):10310–10319
47. Rubin M, Medeiros-Ribeiro G, O'shea J et al (1996) Imaging and spectroscopy of single InAs self-assembled quantum dots using ballistic electron emission microscopy. Phys Rev Lett 77 (26):5268